LETTER

Controlled fragmentation of multimaterial fibres and films via polymer cold–drawing

Soroush Shabahang[1], Guangming Tao[1], Joshua J. Kaufman[1], Yangyang Qiao[2], Lei Wei[3], Thomas Bouchenot[2], Ali P. Gordon[2], Yoel Fink[4], Yuanli Bai[2], Robert S. Hoy[5] & Ayman F. Abouraddy[1,6]

Polymer cold-drawing[1–4] is a process in which tensile stress reduces the diameter of a drawn fibre (or thickness of a drawn film) and orients the polymeric chains. Cold-drawing has long been used in industrial applications[5–7], including the production of flexible fibres with high tensile strength such as polyester and nylon[8,9]. However, cold-drawing of a composite structure has been less studied. Here we show that in a multimaterial fibre[10,11] composed of a brittle core embedded in a ductile polymer cladding, cold-drawing results in a surprising phenomenon: controllable and sequential fragmentation of the core to produce uniformly sized rods along metres of fibre, rather than the expected random or chaotic fragmentation. These embedded structures arise from mechanical–geometric instabilities associated with 'neck' propagation[2,3]. Embedded, structured multimaterial threads with complex transverse geometry are thus fragmented into a periodic train of rods held stationary in the polymer cladding. These rods can then be easily extracted via selective dissolution of the cladding, or can self-heal by thermal restoration to re-form the brittle thread. Our method is also applicable to composites with flat rather than cylindrical geometries, in which case cold-drawing leads to the break-up of an embedded or coated brittle film into narrow parallel strips that are aligned normally to the drawing axis. A range of materials was explored to establish the universality of this effect, including silicon, germanium, gold, glasses, silk, polystyrene, biodegradable polymers and ice. We observe, and verify through nonlinear finite-element simulations, a linear relationship between the smallest transverse scale and the longitudinal break-up period. These results may lead to the development of dynamical and thermoreversible camouflaging via a nanoscale Venetian-blind effect, and the fabrication of large-area structured surfaces that facilitate high-sensitivity bio-detection.

When a longitudinal tensile stress is applied to a ductile polymer fibre or sheet, the mechanical instability known as 'necking' reduces the transverse dimensions of the sample and longitudinally orients the constituent chains[2–4]. The necked region is initially localized, but expands uniformly via propagation of the 'shoulder' into undeformed regions of the polymer until the neck is fully developed and extends throughout the sample length (Fig. 1). The polymer is consequently left in a new, anisotropic phase with potentially superior mechanical and/or optical properties[1,5]. For example, in the original observation of cold-drawing[1], a highly oriented, transparent and robust neck developed in an initially opaque and brittle polyester fibre. Commercial applications that exploited the large tensile strength, low weight and high flexibility of cold-drawn synthetic polymer fibres soon followed[5–7]. After decades of experimental and theoretical research[1–9], cold-drawing is now reasonably well-understood at a phenomenological level.

To date, investigations of cold-drawing have focused on the changes that occur in monolithic structures (composed of a single material)

upon propagation of the shoulder, as well as further deformation leading to material failure[4]. Studies of the cold-drawing of polymer composites have primarily concentrated on improving the mechanical properties of bulk materials via fibre reinforcement[12–14]. Conversely, the study of fibre-reinforced composites has concentrated on fracture phenomena driven by stress-transfer in a matrix[15–17]. Here we report a new dynamical phenomenon that exploits cold-drawing in multimaterial composite structures—in the form-factor of a cylindrical fibre or a flat film (Fig. 1b–d)—and combines disparate materials, only one of which (a thermoplastic polymer) is amenable to cold-drawing. The mechanical–geometric mismatch between the ductile polymer (which undergoes cold-drawing) and the other, relatively brittle material (which does not) is harnessed as a scalable, mechanical pathway to produce a wide variety of complex multi-component nano- and microstructures with arbitrary cross-sectional geometries through the controllable local fragmentation of the brittle materials within the axially propagating polymer shoulders.

We start by describing our observations in the context of the cylindrical multimaterial fibre shown in Fig. 1e, f. The fibre consists of a 20-μm-diameter glass core (the inorganic chalcogenide glass As_2Se_3) embedded in a 1-mm-diameter polymer cladding (the thermoplastic polymer polyethersulfone, PES)[10,11]. Fibres can be tens of metres in length; see Supplementary Information for fibre fabrication. The use of PES is not required; we have reproduced our results in fibres made of other thermoplastic polymers, including polycarbonate, polyetherimide, polysulfone and cyclic olefin polymer. At room temperature, the core is brittle whereas the polymer is ductile. At a homogeneous uniaxial extension of a few per cent, necks form locally and extend until the fibre is fully drawn. Videos capturing the neck expansion and shoulder propagation along the fibre in real time reveal a surprising dynamical phenomenon that takes place inside the polymer shoulders during their propagation along the fibre (Supplementary Video 1). Although the core is initially intact along the fibre axis, within the propagating shoulder the glassy core fragments in an orderly sequence (upon passage of the shoulder) into a periodic train of cylindrical rods that are held stationary in the fibre and separated by voids. As the shoulders propagate further, they continue to fragment the core *in situ* until they consume the whole length of the fibre, or until the applied stress is removed. We harvest the glass micro-rods by selectively dissolving the polymer with an organic solvent (dimethylacetamide, DMAC; Fig. 1g–j); the rough faceted surfaces confirm that the rods result from brittle fracture (Fig. 1j, inset).

This phenomenon is reminiscent of shear-lag fracture (SLF) in fibre-reinforced composites with low interfacial strength[15–17]. SLF is a quite general phenomenon occurring in composites of mechanically incompatible materials. Previous work has generally sought to suppress SLF as a means of increasing the ductility of fibres, whereas here we have induced a controlled form of SLF at the neck front.

[1]CREOL, The College of Optics & Photonics, University of Central Florida, Orlando, Florida 32816, USA. [2]Department of Mechanical and Aerospace Engineering, University of Central Florida, Orlando, Florida 32816, USA. [3]School of Electrical and Electronic Engineering, Nanyang Technological University, Singapore 639798, Singapore. [4]Department of Materials Science and Engineering, Massachusetts Institute of Technology, Cambridge, Massachusetts 02139, USA. [5]Department of Physics, University of South Florida, Tampa, Florida 33620, USA. [6]Department of Materials Science and Engineering, University of Central Florida, Orlando, Florida 32816, USA.
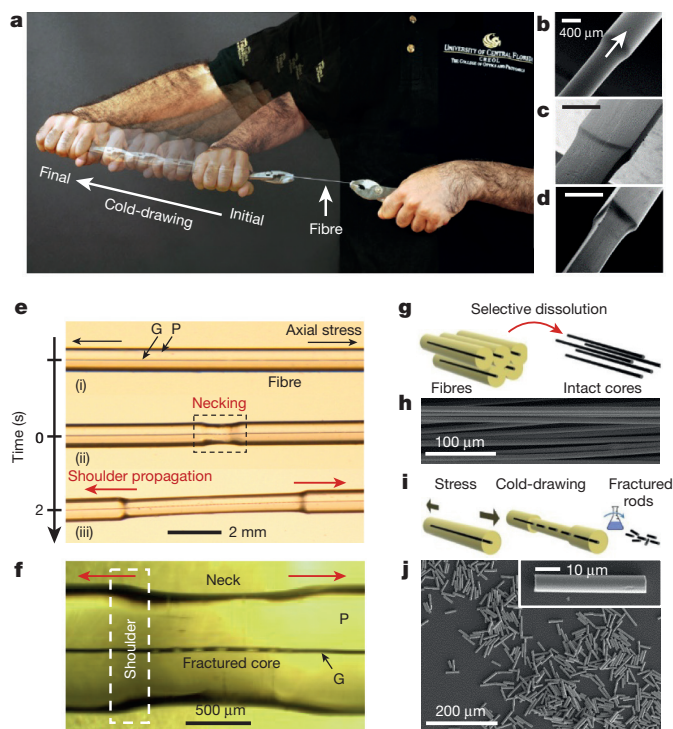
Figure 1 | Fragmentation via a cold-drawing-induced, propagating, mechanical–geometric instability. a, Photograph of a polymer fibre undergoing cold-drawing under axial stress at a speed of approximately 5 mm s^{-1}. Multiple shots taken over 1 min are overlaid to highlight the extent of fibre elongation. **b–d**, Scanning electron microscope (SEM) micrographs of the propagating shoulder in polymer (PES) fibres with cross-sections that are circular (diameter of 0.7 mm; **b**), rectangular (side lengths of 0.2 mm and 1 mm; **c**) and equilaterally triangular (side length of 0.4 mm; **d**). Scale bars, 400 μm. **e**, Transmission optical micrographs of a multimaterial cylindrical fibre undergoing cold-drawing at 3 mm s^{-1} captured at three different stages: (i) initially intact fibre; (ii) neck formation; and (iii) shoulder propagation, leaving behind a fractured core after fragmentation. The cladding is a polymer 'P' (PES) and the core is a glass 'G' (As$_2$Se$_3$). **f**, A magnified transmission micrograph of the neck region, corresponding to the dashed black rectangle in **e**. The dashed white rectangle highlights the propagating instability, wherein fragmentation takes place. **g**, Schematic of selective dissolution of the polymer cladding to retrieve intact cores. **h**, SEM micrograph of retrieved intact glass cores from multiple fibres. **i, j**, Schematic (**i**) and SEM micrograph (**j**) of retrieved nano-fragmented micro-rods by selective dissolution from a cold-drawn fibre. Inset in **j** is an SEM micrograph of a single micro-rod.

Although a 'local' brittle fracture takes place, as in traditional SLF studies, the global dynamics are different; see Extended Data Fig. 1. We have found that this phenomenon applies to many core materials. These materials include dense solids, such as crystalline semiconductors (Si and Ge)[18], and inorganic glasses (such as silicates, phosphates, chalcogenides and tellurites)[19]. Relatively brittle polymers that do not typically undergo cold-drawing themselves can also be fragmented in this manner—including polystyrene, the biodegradable polymer polyethylene oxide, and even natural polymers such as silk and human hair. Indeed, even ice inside a hollow-core polymer fibre undergoes a similar break-up process before melting (Supplementary Fig. S6).

Systematic investigation leads to several non-intuitive findings. First, the average length $\overline{L}$ of the glass rods is linearly proportional to the core diameter D, as shown in Fig. 2a. Second, the linear proportionality $\overline{L}/D = f$ depends on the core material, but not on the details of the experimental procedure (such as drawing speed, pre-stress of the polymer cladding or fibre outer diameter). Specifically, although the values of the strain at which necking is initiated and the final drawing ratio both depend on the fabrication conditions of the fibre, such

as the tension under which it is thermally drawn from the melt (Fig. 2c), they do not affect f. Note that the linear $\overline{L}/D$ proportionality is 'cut off' at an upper limit set by the length of the shoulder region $L_{shoulder}$: it requires that $\overline{L}, D \ll L_{shoulder}, D_{cladding}$, where $D_{cladding}$ is the diameter of the fibre cladding. Third, by determining the ratio f for a wide range of materials (Fig. 2b and Extended Data Table 1), we find empirically that $f \propto \sqrt{E}$, where E is the Young's modulus of the core; for example, As$_2$Se$_3$ cores always have $f \approx 6$, whereas tellurite glass cores have $f \approx 3.9$ (Fig. 2a). Analytic treatments of SLF vary in sophistication from Cox's original heuristic treatment[20] to Nairn's rigorous approach[15], but agree that $\overline{L}/D = \sqrt{E/\Omega}$, consistent with Fig. 2b. Here Ω is a characteristic stress or energy density; for example, Ω is the Young's modulus of the cladding in Cox's theory, whereas later theories yield more complicated expressions for Ω. The data we show in Fig. 2b indicate that $\Omega \approx 0.1$ GPa in our experiments, and the data in Fig. 2c reveal that the true stress within the neck is also approximately 0.1 GPa (our key stress scale).

These results are non-intuitive because stress distributions in the region in which the shoulder meets un-drawn material are known to be complex[21], and the presence of the core introduces additional strain localization due to the mechanical incompatibility between the core and cladding. Some essential features may be captured using a simple Considére model for core fracture in the shoulder region (Fig. 2d). The fragmentation of glass cores may be readily understood as arising from a mechanical–geometric instability. The Considére criterion for necking of solid materials states that undeformed and necked regions coexist. Within the shoulder, complex gradients of these quantities are present, but the brittle fracture of glass cores occurs along the 'coexistence' line shown in Fig. 2d. The specific location along this line at which fracture occurs is material-dependent and sets the ratio f.

Given the above-mentioned complexity of the stress distributions, and to better understand the experimental findings, we perform non-linear finite-element simulations of the cold-drawing process for a typical core/cladding (As$_2$Se$_3$/PES) cylindrical geometry; see Methods. Axisymmetric elements are used and the measured mechanical properties (including elastic modulus, plastic hardening and fracture) of the core and cladding are input to the computational model (Extended Data Fig. 2). The same tensile boundary conditions used in the experiments are applied. The simulation results are illustrated in Fig. 2e with the contour plots of von Mises stress distributions as a function of stretch. In step (ii), necking and core-fracture initiate, with the latter associated with the onset of stress concentration. Necking continues and the shoulders propagate in steps (iii) and (iv), resulting in sequential fragmentation of the core with a length-to-diameter ratio f of the rods that agrees with the experiments (Extended Data Table 2). As the rods pass into the necked region, the increased stretch expands the voids separating the fragments. The final fully drawn configuration is shown in step (v); see Supplementary Video 2 for a video of the simulation, and Extended Data Fig. 1 for a comparison with the more typical stress-transfer fragmentation in fibre-reinforced composites.

As we have demonstrated through cold-drawing of fibres with rectangular and triangular cross-sections (Fig. 1c, d), the phenomena associated with cold-drawing in multimaterial fibres are not restricted to cylindrical geometries. In the flat-fibre geometry, new in-fibre fragmentation phenomena are observed. In particular, when a thin brittle film is embedded in such a fibre (Fig. 3a, b), propagation of the rectangular shoulder upon necking leads progressively to fragmentation of the film into well-ordered strips (Supplementary Video 3). Comparable fracture was reported in ref. 22, in which deformation of metal films on polymer substrates was examined and strategies for maximizing the ductility of these composites were explored. As seen in Fig. 3c, the straight, sharp-edged strips resulting from a glass film fragmenting extend across the width of the fibre (about 1 mm) and are separated by rectangular voids in a well-ordered array extending along the whole fibre length. The optical properties of the flat fibre change markedly as a result of cold-drawing. The undrawn fibre contains
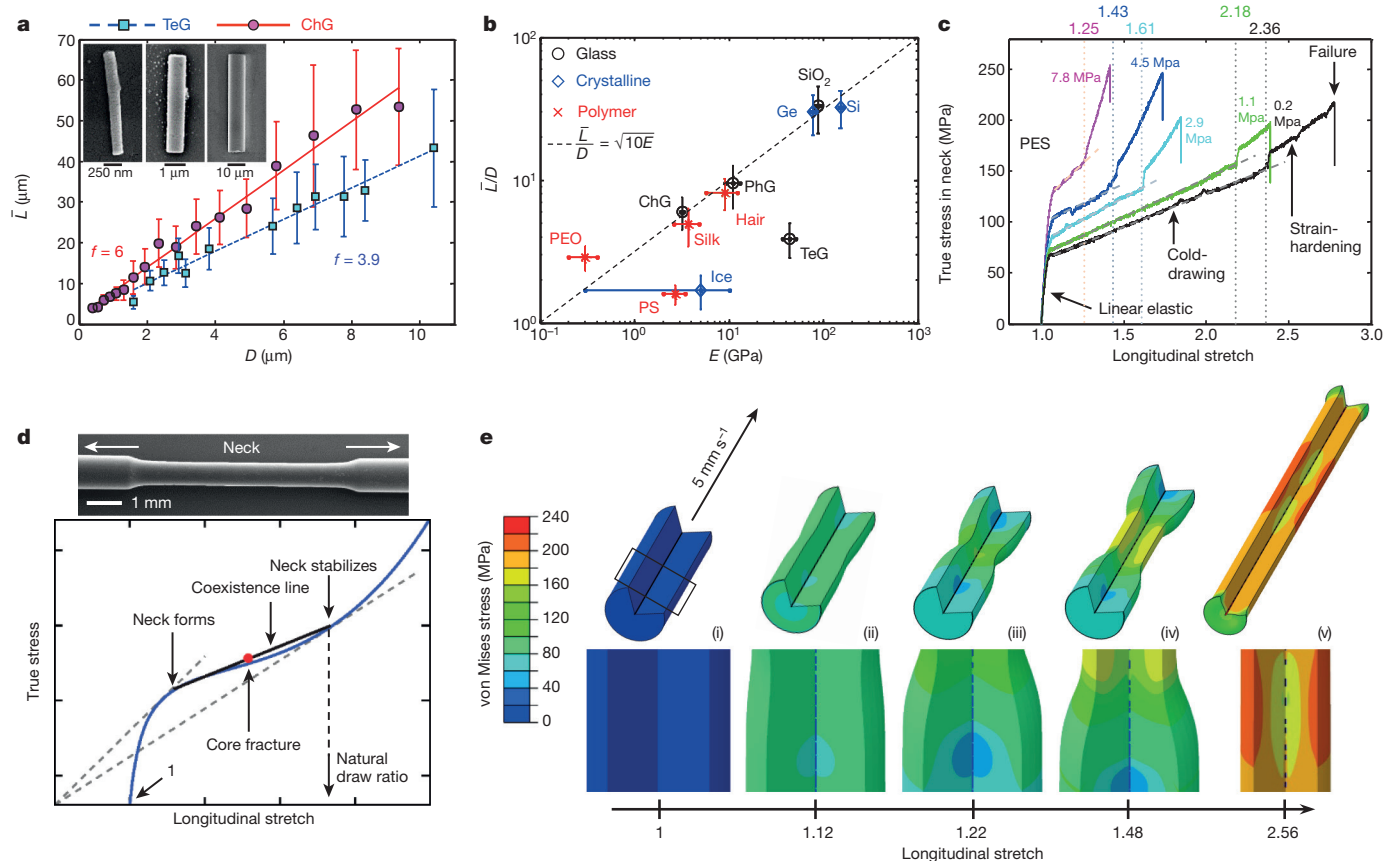
Figure 2 | Characterization of fragmentation induced by cold-drawing of a PES fibre. a, Measurements of the average length $\overline{L}$ of fragmented micro- and nano-rods of chalcogenide glass (ChG; As_2Se_2; red circles) and tellurite glass (TeG; $70TeO_2$–$20ZnO$–$5K_2O$–$5Na_2O$; blue squares) of diameter D in a PES fibre upon cold-drawing. The red solid and blue dashed lines are linear fits with slopes $f = \overline{L}/D = 6$ and 3.9 for ChG and TeG, respectively. Vertical error bars represent the root-mean-squared (r.m.s.) length dispersion of rods at each value of D (Supplementary Information). Insets are SEM micrographs of individual rods resulting from the cold-drawing-driven fragmentation of As_2Se_3 cores of diameters (from left to right) 200 nm, 1 μm and 10 μm. **b,** Measured values of f for a host of materials embedded in a PES fibre plotted against their Young's modulus E; see Extended Data Table 1. The dashed line corresponds to the ansatz $f \approx \sqrt{E/\Omega}$, with $\Omega = 0.1$ GPa (such that $f \approx \sqrt{10E}$ when E is in gigapascals). Vertical error bars represent the measured r.m.s. dispersion in f; horizontal error bars correspond to the uncertainty in the measured E (those for TeG and ice[29] reflect the range of reported values). PhG, phosphate glass; PEO, polyethylene oxide; PS, polystyrene. **c,** Stress–strain measurements of cylindrical PES fibres produced by thermal drawing[30] at different pre-stress values (ranging from 0.2 MPa to 7.8 MPa; see coloured-coded labels) identifying the four stages of linear elasticity, cold-drawing, strain-hardening and failure. The coexistence (dashed) lines and natural draw ratios (vertical dotted lines; values given above the plot) at neck stabilization (both defined in **d**) are identified. **d,** Schematic representation of the Considére model. The blue curve corresponds to the true stress versus stretch in a strain-controlled experiment. The solid black 'coexistence' line indicates necked and unnecked regions coexisting at equal engineering stresses as local stretch varies from the onset of necking to the natural draw ratio at which stable neck propagation occurs. The dashed black lines serve as guides to the eye. Above the plot is an SEM micrograph of a necked region in a PES fibre; the arrows indicate the direction of the axial stress and shoulder propagation. **e,** von Mises stress distributions from finite-element simulations of in-fibre core (As_2Se_3) fragmentation during cold-drawing (at 5 mm s^{-1}) of a PES fibre. The five steps (i)–(v) correspond to increasing stretch values. Top panels depict the full fibre; bottoms panels show the regions corresponding to that highlighted by the rectangle in (i).

a 300-nm-thick, continuous As_2Se_3 film (Fig. 3b), which renders the fibre opaque. Fragmentation (Fig. 3c) reduces the optical opacity as a result of the voids opening up between the strips in the transparent polymer (Fig. 3d, e). Optical spectral transmission measurements reveal a blueshift of approximately 300 nm in the wavelength of the absorption edge after film fragmentation (Fig. 3d). These observations are compared to theoretical predictions for a Fabry–Pérot optical model of the fibre that additionally takes into account absorption, diffraction and Fresnel reflection[23] (Fig. 3e); see Methods. It is important to note that the change in the optical properties upon cold-drawing is a consequence of the mechanical–geometric transformation undergone by the embedded structure and not of the polymer itself.

Figure 3f–k reveals the effect of polymer pre-stress (applied during thermal drawing of the fibre from the melt) on the uniformity and integrity of the fragmented strips. Large pre-stresses (Fig. 3f, i) produce smaller draw ratios[24] (less transverse contraction during neck propagation) and a more uniform stress field within the shoulder, resulting in longer and more-parallel strips. This effect is a consequence of the greater orientation of polymer chains along the thermal drawing direction when compared to fibres drawn at lower pre-stress values. Low pre-stresses result in opposite trends; the film fragmentation is more violent because the strain field is more two-dimensional; that is, both the axial and transverse components are non-negligible. Shear bands in low-melt pre-stressed fibres are expected to play a substantial part in this outcome, which is borne out in finite-element simulations; see Methods, Extended Data Fig. 3, and Supplementary Video 4 for a video of the simulation. We retrieve in our simulations the experimentally observed ratio of strip width to film thickness (Fig. 3f–k) and also observe prominent shear-banding in the polymer that could account for the more violent fragmentation in the case of low pre-stress.

Several unique features of the in-fibre fragmentation process are highlighted in Fig. 4. First, the procedure extends to scenarios in which
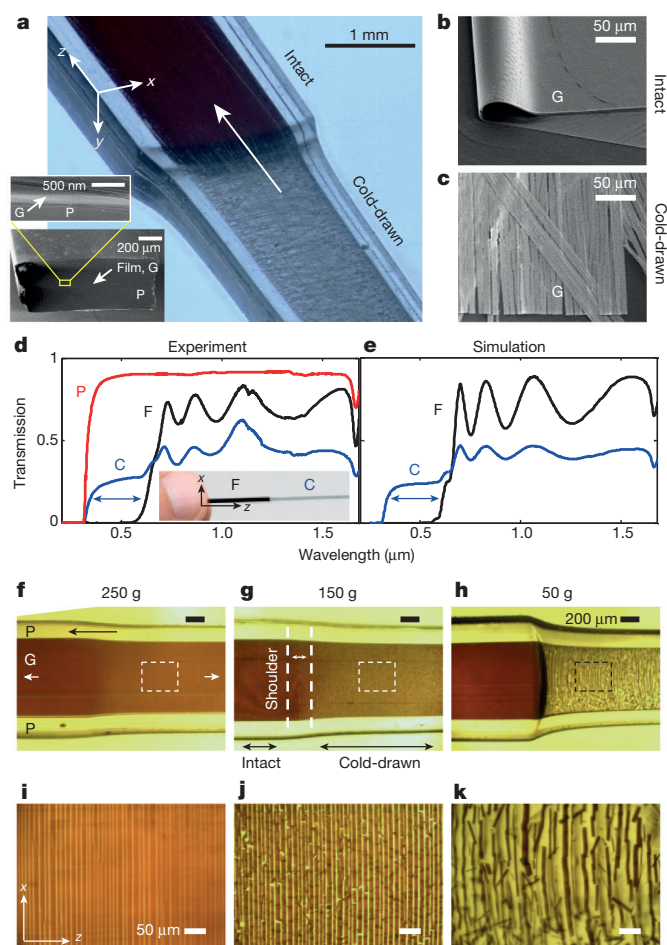
Figure 3 | Fragmentation of a thin film embedded in a flat polymer fibre undergoing cold-drawing. a, Optical micrograph of a flat PES ('P') fibre containing a 300-nm-thick film of As_2Se_3 ('G') (cross-section shown in inset), cold-drawn under axial stress. The propagating flat shoulder in the direction of the arrow separates an intact region (darker colour) and a reduced-size cold-drawn region (lighter colour). **b**, SEM micrograph of intact glass ('G') film retrieved from the fibre before cold-drawing. **c**, SEM micrograph of fragmented glass strips retrieved from the fibre after cold-drawing. **d**, **e**, Measured (**d**) and simulated (**e**) optical transmission through the flat fibre before ('F') and after ('C') cold-drawing. For reference, the transmission through the polymer alone ('P') is plotted in **d**. Inset is a photograph of a section of a fibre showing the change in the optical appearance after cold-drawing-driven fragmentation. **f–h**, Optical transmission micrographs of the necking region for three fibres produced at different pre-stress levels (250 g, **f**; 150 g, **g**; 50 g, **h**). The white arrows indicate the axial stress applied and the back arrow indicates the shoulder-propagation direction. Scale bars, 200 μm. **i–k**, Optical transmission micrographs of the sections in **f–h** enclosed in dashed boxes. Scale bars, 50 μm.

a large number of cores are embedded in a single polymer fibre[25] (about 4,000 cores, each of 500-nm diameter; Fig. 4a). All of the cores simultaneously undergo fragmentation into uniformly sized rods. Thus, this process is readily scalable to large-volume production. Supplementary Video 5 shows an example of a parallelepiped polymer fibre containing six cylindrical As_2Se_3 cores all undergoing fragmentation upon passage of the shoulder. Second, the length-to-diameter ratio may be tuned by using cylindrical shells rather than solid cores (Fig. 4b). Indeed, $\overline{L}/D$ for As_2Se_3, for example, changes from 6 for a solid core (Fig. 2a) to 4.5 and 3.2 when the ratio of the outer to inner diameter of the shell is 4 and 1.5, respectively (Fig. 4c). Here, only the shell undergoes fragmentation, while both the polymer inner core and the cladding are cold-drawn. After dissolving the polymer, hollow glass
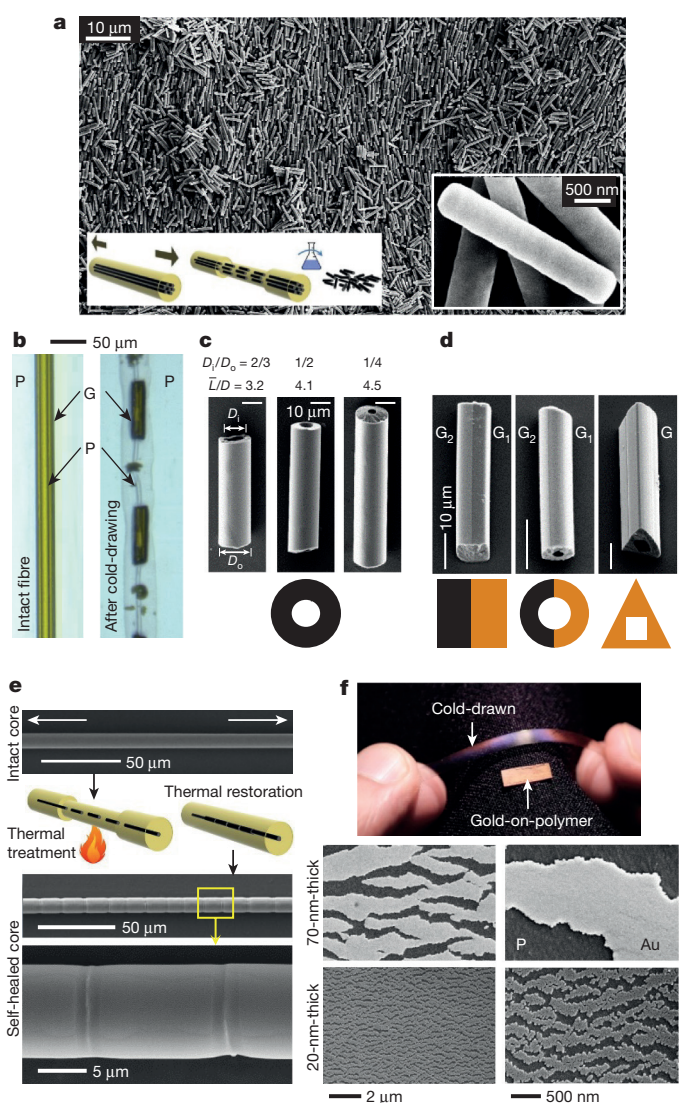

Figure 4 | Characteristics of cold-drawing-driven fragmentation. a, Scalability of the in-fibre process. SEM micrograph of the fragmented rods retrieved from a 1-mm-diameter PES fibre containing about 4,000 500-nm-diameter As_2Se_3 cores after cold-drawing. The left inset is a schematic of the process and the right inset highlights the size of the rods. **b**, Optical transmission micrographs before and after cold-drawing of a fibre whose core has a core-shell structure, with the inner core and cladding both PES ('P') and the shell As_2Se_3 ('G'). Only the shell undergoes fragmentation, while the inner core and cladding are both cold-drawn. **c**, SEM micrographs of single hollow rods retrieved from a fibre such as in **b** with different ratios of inner (polymer-core; D_i) to outer (glass-shell; D_o) diameter. **d**, SEM micrographs of complex particle structures. From left to right, parallelepiped Janus rod, hollow cylindrical Janus rod, and triangular rod with square hole. Scale bars in **c** and **d**, 10 μm. Schematics below the SEM micrographs in **c** and **d** show cross-sections of the structures, with As_2S_3 (G_1) coloured orange and $(As_2Se_3)_{99}Ge_1$ (G_2) coloured black. **e**, Self-healing of glass fragments after thermal restoration. **f**, Photograph showing a polymer film (PES, 'P') with gold (Au) deposited on it before and after cold-drawing. SEM micrographs (left and right columns show two different magnifications) of the fragmented 20-nm-thick and 70-nm-thick gold films.

microtubes are retrieved. Third, the geometry of the micro- or nano-particles produced is limited only by the ability to structure the continuous core. Examples in Fig. 4d include bicompartmental parallelepiped Janus particles, hollow cylindrical Janus particles, and triangular particles with square holes. Such structures are produced

at the macroscopic scale via extrusion and then thermally drawn into a fibre with the desired transverse size; see Supplementary Information for further structures (including solid cylindrical Janus and core-shell particles). Cold-drawing then fragments the structures into particles while maintaining the complex cross-section. Fourth, the fragmentation is thermoreversible (Fig. 4e): heating the drawn fibre above its glass transition temperature results in self-healing of the fragmented core as the initial fibre dimensions are restored. Upon heating the fibre to its softening temperature, the tensile stress is released and the polymer fibre contracts to its initial length via an imperfect shape-memory effect (SME). As voids between the fractured glass segments are eliminated, the segments fuse together (self-heal) and re-form an intact longitudinal core. This effect is not a SME because—by definition—SME can occur only in samples with continuous strain histories.

Further, thermal drawing is not a necessary precursor to producing structures that undergo in-fibre fragmentation. Commercially available polymer films may be directly exploited by coating them with a relatively brittle material. For example, we show in Fig. 4f the fragmentation of a 70-nm-thick gold layer that was sputtered onto a 75-μm-thick PES film. Cold-drawing of this composite results in fragmentation of the gold film into segments with widths of roughly 1.1 μm along the cold-drawing axis (see Extended Data Fig. 4 for the fragmentation of gold films with thicknesses of 20–70 nm). These segments produce a clear optical-diffraction-grating signature that is visually apparent to the naked eye and indicate a grating of period of approximately 2.2 μm, which is consistent with Fig. 4f (see Extended Data Fig. 5 for optical measurements). Alternatively, a dry-erase marker pen can be used to write straight, thick lines (widths of 2–5 mm) on the PES film (Extended Data Fig. 6). The ink interacts with the top layer of the polymer film to form an ∼1-μm-thick brittle crust that fragments upon cold-drawing in a manner similar to that of the gold film.

Cold-drawing has been a mainstay of mass-production of continuous threads in the synthetic fibre and textile industries over most of the past century. It is a fundamental mechanical phenomenon that extends to the processing of macroscale metals[26,27] and nanocrystals[28]. We have shown that this process can be exploited to fabricate discontinuous three-dimensional arrays of multimaterial micro- and nanostructures. Our results suggest potential applications of cold-drawing in controlling the optical properties of macroscopic composite structures through dynamical and thermoreversible nanoscale mechanical processes. This may lead to dynamical camouflaging via a nanoscale Venetian-blind effect, scalable fabrication of micro- and nanoparticles with arbitrary cross-sections, and large-area meta-surfaces for highly sensitive detection of pathogens.

Online Content Methods, along with any additional Extended Data display items and Source Data, are available in the online version of the paper; references unique to these sections appear only in the online paper.

1. Carothers, W. H. & Hill, J. W. Studies of polymerization and ring formation. XV. Artificial fibers from synthetic linear condensation superpolymers. *J. Am. Chem. Soc.* **54,** 1579–1587 (1932).
2. Vincent, P. I. The necking and cold-drawing of rigid plastics. *Polymer* **1,** 7–19 (1960).
3. Coleman, B. D. On the cold drawing of polymers. *Comput. Math. Appl.* **11,** 35–65 (1985).
4. Argon, A. S. *The Physics of Deformation and Fracture of Polymers* Ch. 10 (Cambridge Univ. Press, 2013).
5. Carothers, W. H. Synthetic fiber. US patent 2,130,948 (1938).
6. Marshall, I. & Thompson, A. B. Drawing synthetic fibres. *Nature* **171,** 38–39 (1953).
7. Hermes, M. *Enough for One Lifetime: Wallace Carothers, Inventor of Nylon* (Chemical Heritage Foundation, 1996).
8. Ziabicki, A. *Fundamentals of Fibre Formation: The Science of Fibre Spinning and Drawing* (Wiley, 1976).
9. Carraher, C. E. Jr. *Introduction to Polymer Chemistry* 3rd edn (CRC Press, 2012) edition.
10. Abouraddy, A. F. *et al.* Towards multimaterial multifunctional fibres that see, hear, sense and communicate. *Nature Mater.* **6,** 336–347 (2007).
11. Tao, G., Stolyarov, A. M. & Abouraddy, A. F. Multimaterial fibers. *Int. J. Appl. Glass Sci.* **3,** 349–368 (2012).
12. Loos, J., Schimanski, T., Hofman, J., Peijs, T. & Lemstra, P. J. Morphological investigations of polypropylene single-fibre reinforced polypropylene model composites. *Polymer* **42,** 3827–3834 (2001).
13. Friedrich, K. *et al.* Microfibrillar reinforced composites from PET/PP blends: processing, morphology and mechanical properties. *Compos. Sci. Technol.* **65,** 107–116 (2005).
14. Fakirov, S., Bhattacharyya, D., Lin, R. J. T., Fuchs, C. & Friedrich, K. Contribution of coalescence to microfibril formation in polymer blends during cold drawing. *J. Macromol. Sci. B* **46,** 183–194 (2007).
15. Nairn, J. A. On the use of shear-lag methods for analysis of stress-transfer in unidirectional composites. *Mech. Mater.* **26,** 63–80 (1997).
16. Asloun, Ei. M., Nardin, M. & Schultz, J. Stress transfer in single-fibre composites: effect of adhesion, elastic modulus of fibre and matrix, and polymer chain mobility. *J. Mater. Sci.* **24,** 1835–1844 (1989).
17. Wang, X., Zhang, B., Du, S., Wu, Y. & Sun, X. Numerical simulation of the fiber fragmentation process in single-fiber composites. *Mater. Des.* **31,** 2464–2470 (2010).
18. Ballato, J. *et al.* Silicon optical fiber. *Opt. Express* **16,** 18675–18683 (2008).
19. Tao, G. *et al.* Infrared fibers. *Adv. Opt. Photon.* **7,** 379–458 (2015).
20. Cox, H. L. The elasticity and strength of paper on other fibrous materials. *Br. J. Appl. Phys.* **3,** 72–79 (1952).
21. Boyce, M. C., Montagut, E. L. & Argon, A. S. The effects of thermomechanical coupling on the cold drawing process of glassy polymers. *Polym. Eng. Sci.* **32,** 1073–1085 (1992).
22. Lu, N., Suo, Z. & Vlassak, J. J. The effect of film thickness on the failure strain of polymer-supported metal films. *Acta Mater.* **58,** 1679–1687 (2010).
23. Saleh, B. E. A. & Teich, M. C. *Fundamentals of Photonics* 2nd edn (Wiley, 2007).
24. Zartman, G. D. *et al.* How melt-stretching affects mechanical behavior of polymer glasses. *Macromolecules* **45,** 6719–6732 (2012).
25. Kaufman, J. J. *et al.* Thermal drawing of high-density macroscopic arrays of well-ordered sub-5-nm-diameter nanowires. *Nano Lett.* **11,** 4768–4773 (2011).
26. Stören, S. & Rice, J. R. Localized necking in thin sheets. *J. Mech. Phys. Solids* **23,** 421–441 (1975).
27. Bai, Y. & Wierzbicki, T. Forming severity concept for predicting sheet necking under complex loading histories. *Int. J. Mech. Sci.* **50,** 1012–1022 (2008).
28. Fang, T. H., Li, W. L., Tao, N. R. & Lu, K. Revealing extraordinary intrinsic tensile plasticity in gradient nano-grained copper. *Science* **331,** 1587–1590 (2011).
29. Schulson, E. M. The structure and mechanical behavior of ice. *J. Miner. Met. Mater. Soc.* **51,** 21–27 (1999).
30. Li, T. (ed.). *Optical Fiber Communications: Fiber Fabrication* Vol. 1 (Academic Press, 1985).

Author Contributions S.S. and A.F.A. developed and directed the project. S.S. observed the cold-drawing-related phenomena, carried out the break-up experiments in fibres and films, produced the hybrid samples based on hollow-core polymer fibres, and performed the optical measurements, the particle length measurements and the thermal restoration experiments. G.T. extruded the multimaterial preforms, fabricated the stack-and-draw preforms and produced all the chalcogenide-polymer and tellurite-polymer fibres. J.J.K. carried out the SEM imaging and produced the hollow-core polymer fibres and the multi-core fibres. Y.Q. and Y.B. carried out the finite-element simulations. L.W. and Y.F. produced the thin glass films and the Si and Ge micro-wires. T.B., S.S. and A.P.G. performed the stress–strain measurements and recorded the Supplementary Videos. R.S.H. developed the heuristic analytical model. Y.F., Y.B., R.S.H. and A.F.A. supervised the research. S.S., Y.B., R.S.H. and A.F.A. wrote the paper. All authors contributed to the interpretation of the results.

Author Information Reprints and permissions information is available at www.nature.com/reprints. The authors declare no competing financial interests. Readers are welcome to comment on the online version of the paper. Correspondence and requests for materials should be addressed to A.F.A. (raddy@creol.ucf.edu).

METHODS

Fibre fabrication. The polymer cylindrical (Figs 1 and 2) and flat (Fig. 3) PES fibres are produced by thermal drawing in a custom-built fibre draw tower. In case of core materials that are thermally compatible with PES (that is, they soften in an overlapping temperature range in which they have comparable viscosity[10,11]), such as chalcogenide and tellurite glasses, the polymer cladding and glass core are co-drawn into a fibre from a centimetre-scale 'preform'. The fibre pre-stress is set during the thermal drawing process; thermal drawing is followed by a rapid quench. In the case of all other materials that are not thermally compatible with PES, microfibres of these materials are first prepared (see Supplementary Information) and then placed within a hollow-core PES fibre, which is thermally drawn from a hollow preform. The fibre assembly is heated to enable collapse of the PES around the core material and thus to produce strong adhesion between PES and the core.

Thin-film preparation. The glassy chalcogenide films (Fig. 3) used are thermally evaporated under vacuum onto a thin PES film that is then incorporated into a flat preform, thermally consolidated under vacuum, and subsequently drawn into a fibre. The gold films (Fig. 4f) are deposited using a sputtering system (Cressington 108) onto commercially available 75-μm-thick PES thin films (Ajedium). The thickness of the gold is controllable up to 50 nm by varying the sputter time. Multiple sputtering procedures are performed to achieve thicknesses exceeding 50 nm.

Stress–strain measurements. Stress–strain measurements of the fibres are gathered from uniaxial tension testing performed via an Instron universal test machine with a load cell resolution of ±0.01 N and the specimen ends are fixed using TestResources wave-type grips. The initial clear length of the fibre between the two grips is typically at least 20 cm. Each test is conducted under displacement-control of 10 mm min^{-1} to rupture.

Simulations for cylindrical fibres. The Explicit solver of the general-purpose finite-element code ABAQUS[31] is used for the computational analysis of the cold-drawing and fragmentation processes. For the cylindrical fibres (Fig. 2e), an axisymmetric model is built using CAX4R elements[31] (5 μm × 5 μm) consisting of three concentric 2.52-mm-long cylindrical layers (Extended Data Fig. 2a). The inner section (10-μm radius) corresponds to the core material, the cladding section (500-μm radius) to the PES matrix. The stress–strain curve for PES (Extended Data Fig. 2b) is based on the test data (Fig. 2c). These two layers are separated by an interfacial layer[32] that possesses similar properties to PES, but with much weaker strength; we thus take the stress–strain curve for this interfacial layer to be the same as for PES, but multiplied by a scalar factor that depends on the core material. Extended Data Fig. 2c shows the stress–strain curve for the interfacial layer when the core is As$_2$Se$_3$. For the core section, we use a brittle-cracking failure model[33] available in ABAQUS, which includes a linear elastic range (taken from test data; see Supplementary Fig. 14f) and softening behaviour at crack propagation. We use an explicit code to predict necking in the PES cladding[34–36]. Specifically, we use the elastic-viscoplastic continuum model proposed in ref. 36. The model is calibrated with respect to the test data and implemented in ABAQUS using the material subroutine VUMAT. In the simulations, the lower grip is fixed and the upper grip is assigned a constant velocity of 5 mm s^{-1} upwards. Simulations are conducted for multiple core materials, including As$_2$Se$_3$ (Extended Data Fig. 2d), Si (Extended Data Fig. 2e), Ge and polystyrene. The results are summarized in Extended Data Table 2. The average length-to-diameter ratios $\bar{L}/D$ of fragmented rods and their standard deviations correlate well with the measurements (Fig. 2b).

Simulations for flat fibres. The flat-fibre cold-drawing simulations are carried out using a similar procedure to that for the cylindrical-fibre simulations. A plane-strain model is built in the plane spanned by the longitudinal axis of the fibre and the fibre thickness (y–z plane in Fig. 3a). This is a good approximation for the thin film because the strain in the transverse direction is much smaller than that in the other two directions during cold-drawing. A quarter of the cross-section is modelled using symmetric boundary conditions, using CPE4R elements[31] approximately 75 nm × 1,000 nm in size. There are three sections defined in the simulation: the film, an interfacial layer and the outer PES cladding. The dimensions used in the simulation (Extended Data Fig. 3) are the same as those in the experiment (Fig. 3a): the film and fibre thicknesses are 300 nm and 350 μm, respectively, and the initial fibre length is 1.44 mm. The material models used are the same as those used in the cylindrical cold-drawing simulations above (Extended Data Fig. 2). The moving grip applies a constant tensile velocity of 2 mm s^{-1}. Extrusion and mirror methods[31] are used to visualize the results in three dimensions. The width of the fragmented strips in the cold-drawing simulation is 7.55 μm, which is in good agreement with the measurements.

Animations. Supplementary Videos 2 and 4 show simulations of the cylindrical fibre and of the flat fibre, respectively. In each video, the frames of the above-described simulations are assembled, in addition to a view of the insets shown in Fig. 2e (for the cylindrical fibre) and Extended Data Fig. 3 (for the flat fibre). In both videos, the speed of the frames is reduced by a factor of 100 compared to the time steps of the simulation drawing speed.

Optical model for transmission through fragmented glass films. We consider an optical model of the flat fibre in Fig. 3a consisting of a 300-nm-thick film of As$_2$Se$_3$ embedded in a 300-μm-thick, 2-mm-wide rectangular PES fibre (Fig. 3a). The refractive index of PES $n_p(\lambda)$ is extracted from spectroscopic ellipsometry measurements in the wavelength range $\lambda = 0.35$–5 μm. The refractive index of the glass $n_g(\lambda)$ is obtained from a Sellmeier equation[37] and experimentally confirmed by ellipsometric measurements, while spectral absorption in the visible range is obtained from optical transmission measurements; optical transmission through the thin glass film is negligible when $\lambda < 0.5$ μm. The glass–polymer interfaces give rise to optical-field Fresnel reflection and transmission coefficients $r_{pg}(\lambda)$ and $t_{pg}(\lambda)$; the two air–polymer interfaces contribute a transmission coefficient $t_p(\lambda)$. Transmission through the intact flat fibre is $T_{intact} = |t_p|^2 |t_{pg}|^2 |1 + r_{pg}^2 e^{i\frac{4\pi}{\lambda}n_g d}|^2$, in which d is the thickness of the glass film and we have taken into consideration only the first two Airy wavelets in the lossy Fabry–Perot resonator formed of the glass film (absorption in the film diminishes the effect of higher-order reflected wavelets). Transmission through a cold-drawn sample embedding the fragmented glass strips is calculated by weighing the transmission through an intact sample T_{intact} and the transmission through a polymer sample $T_p = |t_p|^2$ with respect to the relative areas of the fragmented strips and the voids separating them. If we define δ to be the ratio of the width of a void separating two strips to the width of a strip, then the transmission through the cold-drawn sample is $T = (\alpha T_p + \beta T_{intact})\eta_{diff}$, in which $\alpha = \frac{1}{1+\delta}$, $\beta = 1 - \alpha$, $\eta_{diff}(\lambda) = \frac{\int_{det} I(x)\mathrm{d}x}{\int_{total} I(x)\mathrm{d}x}$ is the fraction of light diffracted through the evenly spaced glass strips that reaches the detector aperture as function of wavelength, and $I(x)$ is the intensity distribution in the detector plane. Using the measured values of the refractive indices of the fibre materials in these formulae, we calculate the theoretical optical transmission spectra plotted in Fig. 3e.

Diffraction measurements on fragmented gold films. The gold–PES cold-drawn samples diffract transmitted (and reflected, Fig. 4f) white light, leading to angular-selective visible colours. To quantify this observation, the diffracted spectra are measured in transmission mode as a function of the angle with respect to the axis defined by normal incidence. A broadband, incoherent, white-light optical source is coupled into a multimode optical fibre by means of a fibre collimator, and out-coupled light is collimated using a ×4 microscope objective lens. The 5 mm × 20 mm sample is placed at a distance of 10 cm from the lens, whereupon the beam diameter is approximately 4 mm. Diffracted light at angle θ is coupled into a multimode fibre via a lens with a 50-mm focal length, and the spectra are recorded using an optical spectrum analyser (OSA; Advantest Q8381A); see Extended Data Fig. 5a. The diffracted light is blueshifted at small angles and redshifted at large angles (Extended Data Fig. 5b).

Assuming normal incidence on the film, the ideal grating equation indicates that $\lambda = \Lambda\sin(\theta)$, in which λ is the wavelength, Λ is the grating period and θ is the diffraction angle of the first diffraction order with respect to the normal to the film. We identify θ with the peak diffracted wavelength λ_{max} in Extended Data Fig. 5b, so that we have the following pairings (λ_{max}, θ): (420 nm, 10.6°), (700 nm, 17.4°) and (800 nm, 21.2°). These measurements indicate grating periods Λ of 2.3 μm, 2.34 μm and 2.21 μm, respectively, which are consistent with the SEM micrographs in Fig. 4f.

Preparing ink-written films for cold-drawing. The ink–PES samples are prepared by cutting a 75-μm-thick PES film (Ajedium) into strips with dimensions of about 5 mm × 10 cm. Using a black permanent marker, thick lines (approximately 2–5-mm thick) are painted on one face of the strips. The marker tip is traced on the PES film only once to avoid non-uniformities in the ink layer left on the film surface (Extended Data Fig. 6a). The samples are dried for a few seconds and then cold-drawn by symmetrically pulling both ends using a pair of pliers (Extended Data Fig. 6b). The optical appearance of the film (Extended Data Fig. 6c) changes immediately after cold-drawing, whereupon bright coloured optical diffraction bands are visible to the eye. SEM micrographs of the surface of the film (Extended Data Fig. 6d, e) reveal that the ink absorbed at the surface of the film produces a crust with an average thickness of <1 μm. The thickness of the crust tapers at the edges of the drawn line. We find that the ink crust after cold-drawing fragments into strips whose width is proportional to the crust thickness. The ink-crust strips are parallel and aligned orthogonally to the cold-drawing axis (the long dimension of the polymer strip), similarly to the observations in Fig. 3 with the glass films embedded in a flat polymer fibre. Thus, at the edge of the line where the thickness drops rapidly, we concomitantly observe a rapid drop in the width of the strips (Extended Data Fig. 6e).

Cold-drawing break-up versus stress transfer in fibre-reinforced composites. The results presented here are related to the shear-lag fracture (SLF) phenomena

often observed in fibre-reinforced composites. However, the fragmentation we report is distinct from canonical SLF in both aim and character, as follows.

(1) In traditional composites, the role of the core is to strengthen the fibre. By contrast, our goal is to exploit the cold-drawing process to produce controlled fragmentation of the core. In other words, we exploit SLF rather than seeking to avoid it as has been the focus of most previous work.

(2) There are several aspects that distinguish the SLF process reported here from canonical SLF. Since the seminal work by Cox[20], the standard theoretical frameworks for analysing stress transfer in composites have used uniaxial models. Most treatments have assumed that there is no load transfer at the fibre ends because they are both 'free'. By contrast, our fibres are semi-infinite; fracture occurs at the free end, while the other end remains tethered to the remainder of the core. More fundamentally, cold-drawing necessarily produces non-trivial multi-axial stresses[4,21], especially in thin films[22]. We expect that these distinguishing features will stimulate future theoretical and experimental investigations into SLF.

(3) In contrast to canonical SLF where fragmentation typically occurs simultaneously in many locations, our core fibres fragment only within the advancing neck front. Once a fragment of the core is separated, it does not undergo any further fracture.

(4) Core fracture occurs as the core passes through the propagating shoulder, producing multimaterial rods of controllable length. Alternatively, when one of the materials making up the core is the same polymer used as the cladding, this portion of the core/fibre undergoes cold-drawing and remains intact while the remaining materials fracture. This feature enables the production of hollow structures via selective dissolution of polymer.

Extended Data Fig. 1 illustrates the distinction between SLF that takes place in the process reported here and in tradition fibre-reinforced composites. The nature of each fracture event taking place during the necking of the polymer fibres is the same as that occurring in SLF in composite materials. In both cases, a local brittle fracture takes place. The fundamental difference lies in the global dynamics of the break-up process.

Traditional SLF. In the case of traditional SLF[38–41] (Extended Data Fig. 1b), the setting is typically that of a composite material, usually fibres in a matrix (what we call core in a cladding). When axial stress is applied, random brittle fractures occur along the fibres. This process continues as long as the stress is applied or until a minimum size of the fractured fibre segments is reached. If the stress is removed before saturation is reached, then what remains is a collection of fibre fragments of unequal, random lengths. Re-applying the axial stress leads to a continuation of the brittle fracture (still localized in the shoulder) until saturation. Post-saturation, the axial stress does not lead to further fracture.

Fragmentation during cold-drawing. In the case of fragmentation during cold-drawing (Extended Data Fig. 1a), the polymer cladding (or matrix) undergoes necking that is by and large independent of the brittle core. During the propagation of the neck upon axial stress, the core undergoes brittle fracture in an orderly fashion on a global scale: the fracture occurs sequentially within the moving shoulder. This process continues as long as the axial stress is applied or until the fibre becomes fully drawn. If the axial stress is removed before the fibre is fully drawn, then we are left with a section of the core that is intact and that has not undergone fracture (the section with the undrawn polymer), and a section that has fractured in a periodic sequence of equally sized fragments (the drawn section of the polymer fibre). Re-applying the axial stress results in a continuation of necking and resumption of the associated fragmentation. After the fibre is fully drawn, no more fragmentation takes place.

31. ABAQUS User's Manual, version 6.11 (Simulia, Inc., 2011).
32. Mital, S. K., Murthy, P. L. N. & Chamis, C. C. Interfacial microfracture in high temperature metal matrix composites. *J. Compos. Mater.* **27,** 1678–1694 (1993).
33. Hillerborg, A., Modéer, M. & Petersson, P.-E. Analysis of crack formation and crack growth in concrete by means of fracture mechanics and finite elements. *Cement Concr. Res.* **6,** 773–781 (1976).
34. Hutchinson, J. W. & Neale, K. W. Neck propagation. *J. Mech. Phys. Solids* **31,** 405–426 (1983).
35. Neale, K. W. & Tuğcu, P. Analysis of necking and neck propagation in polymeric materials. *J. Mech. Phys. Solids* **33,** 323–337 (1985).
36. Anand, L. & Gurtin, M. E. A theory of amorphous solids undergoing large deformations, with application to polymeric glasses. *Int. J. Solids Struct.* **40,** 1465–1487 (2003).
37. Ung, B. & Skorobogatiy, M. Chalcogenide microporous fibers for linear and nonlinear applications in the mid-infrared. *Opt. Express* **18,** 8647–8659 (2010).
38. Figueroa, J. C., Carney, T. E., Schadler, L. S. & Laird, C. Micromechanics of single filament composites. *Compos. Sci. Technol.* **42,** 77–101 (1991).
39. Galiotis, G. & Paipetis, A. Definition and measurement of the shear-lag parameter, β, as an index of the stress transfer efficiency in polymer composites. *J. Mater. Sci.* **33,** 1137–1143 (1998).
40. Kim, B. W. & Nairn, J. A. Observations of fiber fracture and interfacial debonding phenomena using the fragmentation test in single fiber composites. *J. Compos. Mater.* **36,** 1825–1858 (2002).
41. Thostenson, E. T., Li, W. Z., Wang, D. Z., Ren, Z. F. & Chou, T. W. Carbon nanotube/carbon fiber hybrid multiscale composites. *J. Appl. Phys.* **91,** 6034–6037 (2002).
42. Kurkjian, C. R. Mechanical properties of phosphate glasses. *J. Non-Cryst. Solids* **263–264,** 207–212 (2000).
43. Chang, K. H., Lee, T. H. & Hwa, L. G. Structure and elastic properties of iron phosphate glasses. *Chin. J. Physiol.* **41,** 414–421 (2003).
44. Rouxel, T. Elastic properties and short- to medium-range order in glasses. *J. Am. Ceram. Soc.* **90,** 3019–3039 (2007).
45. Pérez-Rigueiro, J., Viney, C., Llorca, J. & Elices, M. Mechanical properties of single-brin silkworm silk. *J. Appl. Polym. Sci.* **75,** 1270–1277 (2000).
46. Cheung, H.-Y., Lau, K.-T., Ho, M.-P. & Mosallam, A. Study on the mechanical properties of different silkworm silk fibers. *J. Compos. Mater.* **43,** 2521–2531 (2009).
47. Zhang, K., Si, F. W., Duan, H. L. & Wang, J. Microstructures and mechanical properties of silks of silkworm and honeybee. *Acta Biomater.* **6,** 2165–2171 (2010).
48. Hartouni, E. & Mecholsky, J. J. Mechanical properties of chalcogenide glasses. *Proc. SPIE* **0683,** 92–97 (1986).
49. Littler, I. C. M., Fu, L. B., Mägi, E. C., Pudo, D. & Eggleton, B. J. Widely tunable, acousto-optic resonances in chalcogenide As$_2$Se$_3$ fiber. *Opt. Express* **14,** 8088–8095 (2006).
50. Tanaka, K. & Shimakawa, K. *Amorphous Chalcogenide Semiconductors and Related Materials* (Springer, 2011).
51. El-Mallawany, R. A. H. *Tellurite Glasses Handbook: Physical Properties and Data* (CRC Press, 2011).
52. Hu, Z. *et al.* Measurement of Young's modulus and Poisson's ratio of human hair using optical techniques. *Proc. SPIE* **7522,** 75222Q (2010).
53. Kaplan, P. D. *et al.* Grey hair: clinical investigation into changes in hair fibres with loss of pigmentation in a photoprotected population. *Int. J. Cosmet. Sci.* **33,** 171–182 (2011).
54. Nie, H.-Y., Motomatsu, M., Mizutani, W. & Tokumoto, H. Local modification of elastic properties of polystyrene–polyethyleneoxide blend surfaces. *J. Vac. Sci. Technol. B* **13,** 1163–1166 (1995).
55. Bellan, L. M., Kameoka, J. & Craighead, H. G. Measurement of the Young's moduli of individual polyethylene oxide and glass nanofibers. *Nanotechnology* **16,** 1095–1099 (2005).
56. Weeks, W. F. & Assur, A. *The Mechanical Properties of Sea Ice* (US Army Material Command, Cold Regions Research and Engineering Laboratory, 1967).
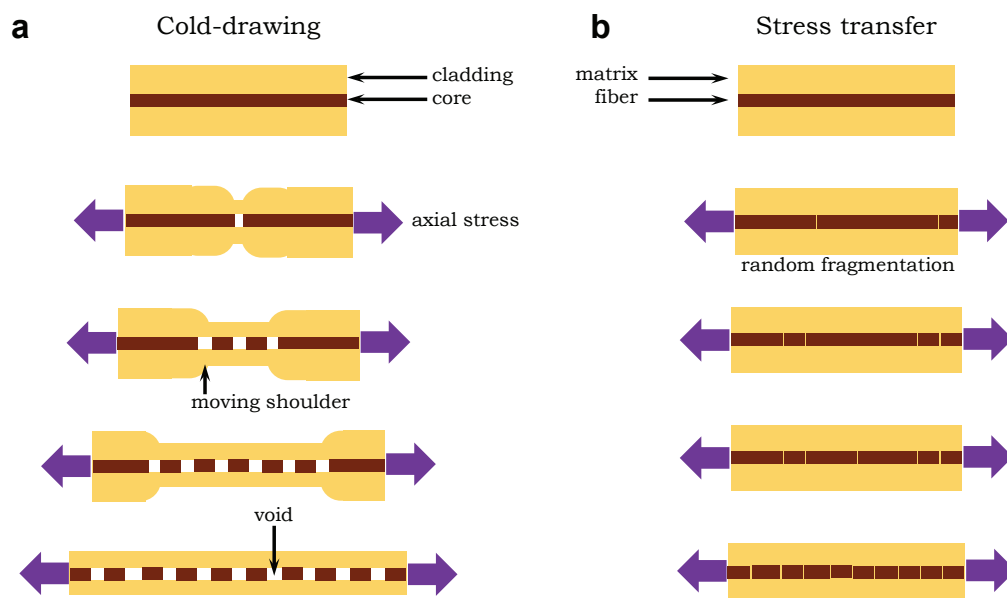
Extended Data Figure 1 | Schematic contrasting controlled (sequential) and uncontrolled (random) thread fragmentation. a, The designed fragmentation process that takes place during cold-drawing of a fibre consisting of a brittle core embedded in a ductile cladding. The overall length of the sample increases considerably when fully drawn. **b**, The random fragmentation that takes place during stress transfer in a composite sample consisting of a fibre embedded in a matrix. Thick purple arrows indicate externally applied stress.
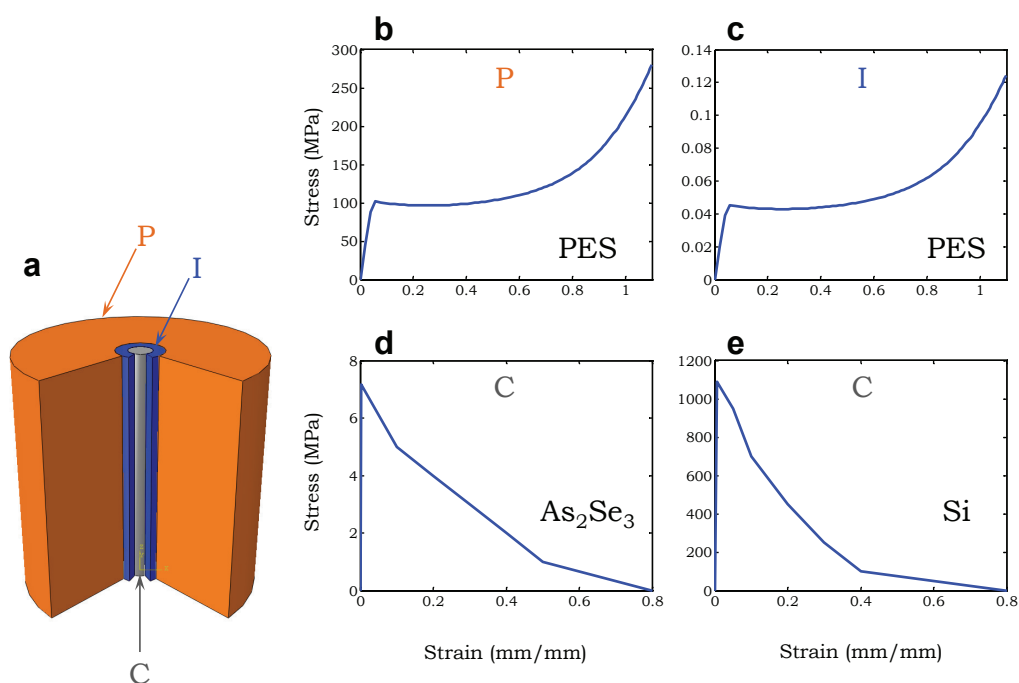
Extended Data Figure 2 | Stress–strain models of the materials used in the finite-element computational model. a, Axisymmetric structure used in the computational model. P, polymer (PES); I, interfacial layer; C, core. The same polymer and interfacial layer are used in the cylindrical and flat fibre simulations. Various core materials are used. **b**, Stress–strain model for the PES cladding ('P' in **a**). **c**, Stress–strain model (including both elastic range and post-failure softening) for the PES interfacial layer ('I' in **a**). **d**, Stress–strain model for an As_2Se_3 core material ('C' in **a**). **e**, Stress–strain model for a silicon (Si) core; see Supplementary Figs 14 and 15.
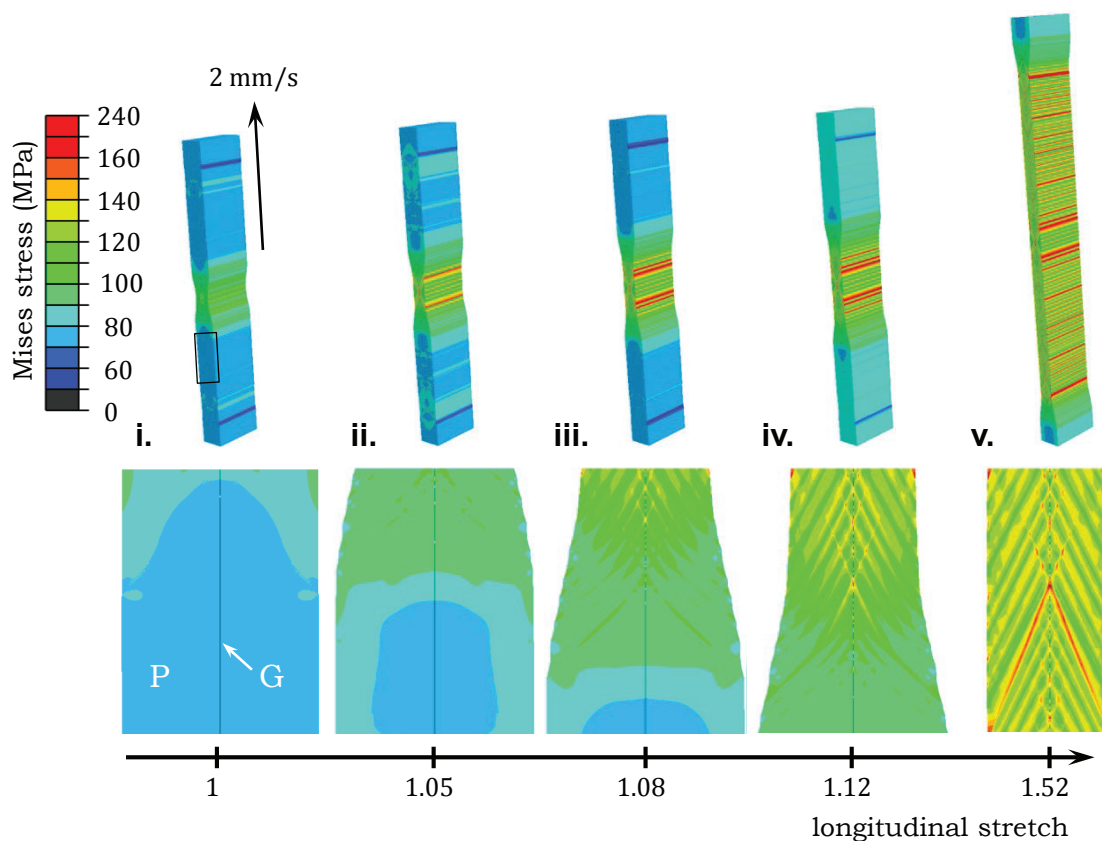
Extended Data Figure 3 | Simulation of cold-drawing in a flat fibre containing a thin brittle film. The results of nonlinear finite-element simulations showing contour plots of the evolving von Mises stress distribution with increasing stretch, using the same (isotropic) materials (PES and As_2Se_3) as in the cylindrical case (Fig. 2e and Extended Data Fig. 2). The five steps (i)–(v) correspond to increasing stretch values. Top panels depict the full fibre; bottoms panels show the regions corresponding to that highlighted by the rectangle in (i). P, polymer (PES); G, glass (As_2Se_3).
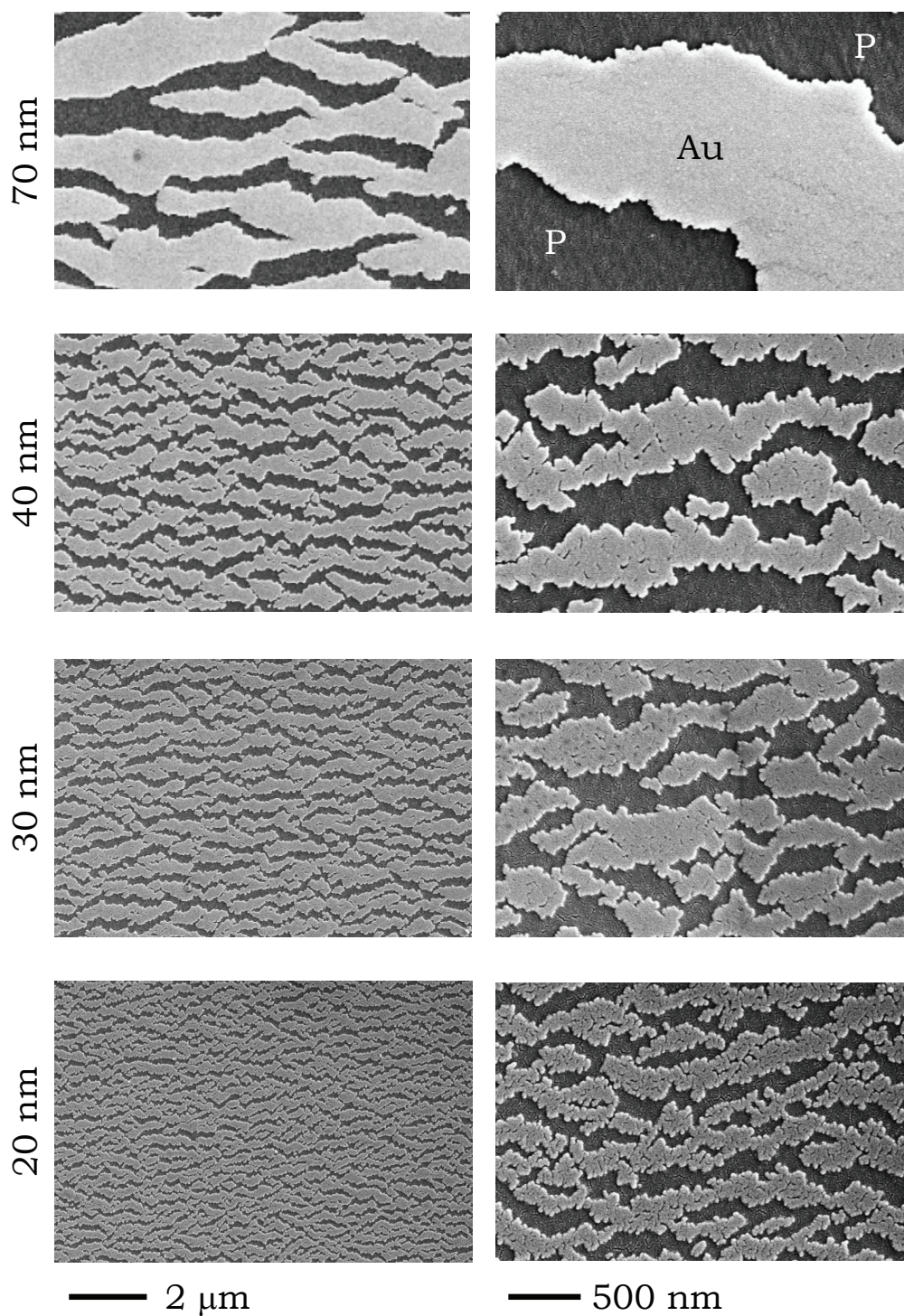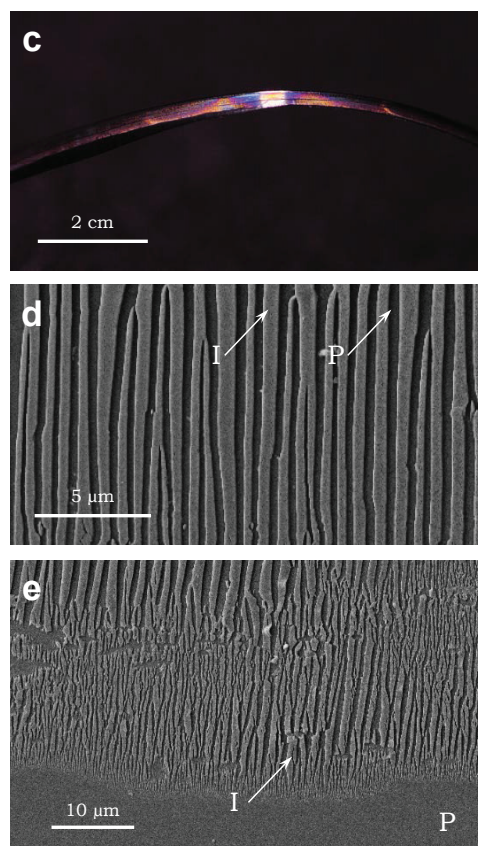
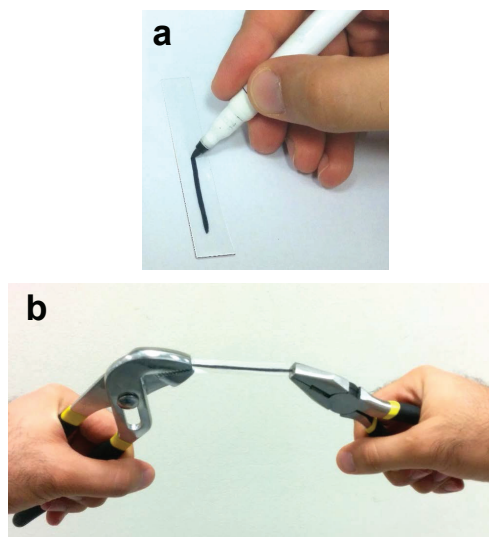**Extended Data Figure 4 | Fragmentation of a gold thin film under cold-drawing.** Each row corresponds to a different thickness of gold (20 nm, 30 nm, 40 nm and 70 nm) sputtered onto a 75-μm-thick PES film. The columns show SEM micrographs of the gold films after cold-drawing at two different scales to highlight the dependence of the average fragment size on the thickness of the gold layer. P, PES film; Au, sputtered gold.
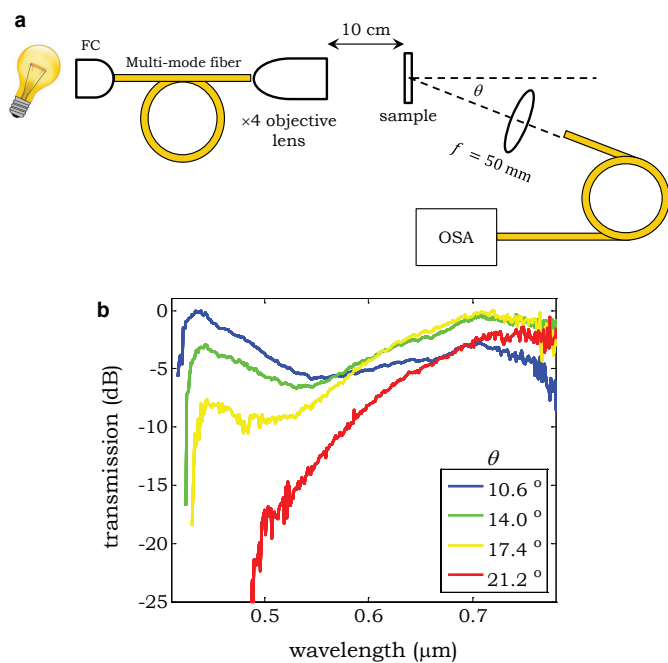
Extended Data Figure 5 | Spectral diffraction measurements from a gold film fragmented by cold-drawing. a, Optical set-up used to measure the spectrum of light diffracted at an angle θ from a thin gold film of thickness 70 nm on a 75-μm-thick PES film after fragmentation via cold-drawing (Extended Data Fig. 4, first row). OSA, optical spectrum analyser; FC, fibre coupler; θ is the angle with respect to normal incidence on the film. **b**, Measured diffracted spectra on a vertical logarithmic scale. The spectra are normalized with respect to the input optical spectrum. Each spectrum is then normalized to its maximum value.

Extended Data Figure 6 | Fragmentation of a layer of ink on PES under cold-drawing. a, **b**, Photographs depicting the cold-drawing procedure. **a**, A line is drawn on a 75-μm-thick PES film (5 mm × 10 cm) using a dry-erase marker pen. **b**, Using two pliers, the two ends of the strip are pulled symmetrically by hand until cold-drawing is complete. **c**, After cold-drawing, the optical appearance of the strip changes and coloured diffracted bands are apparent to the naked eye (the marker pen is used to write across the whole film surface). **d**, SEM micrograph of the drawn line reveals that a crust is formed at the PES surface that fragments into strips that are orthogonal to the cold-drawing axis (similarly to in Figs 3 and 4f), which are behind the new optical properties of the strip seen in **c**. **e**, SEM micrograph of the edge of the drawn line, showing a tapering of the thickness of the ink crust, and concomitant drop in fragmentation period. I, ink-polymer crust; P, PES polymer film.

Extended Data Table 1 | Measured values of $\bar{L}/D$ and measured and reported values of E, for different core materials

Material	$\dfrac{\bar{L}}{D}$	St. Dev.	E (GPa)	Δ (GPa)	E (GPa)	Δ (GPa)
	Measured		Measured		Reported	
SiO_2	33	11.95	88.5	5.5	70	65 – 73.1
Si	32.5	9.56	152	7.5	150	130–202
Ge	30	9.26	78	6	103	102.7–103
PhG[42-44]	9.5	3.19	11	2	55	31.3–79
Silk[45-47]	8.2	2.07	9	3.2	16	3.8–17
ChG[48-50]	6	1.57	3.2	0.1	38.6	18–40
TeG[51]	3.9	1.07	N/A[1]	N/A[1]	44	37.1–50.7
Hair[52,53]	4.9	1.46	3.7	1.1	4	2.5–7.5
PEO[54,55]	2.9	0.56	0.3	0.1	5	0.2–7
Ice[20,44,56]	1.7	0.46	N/A[2]	N/A[2]	5.1	0.3–10
PS	1.6	0.25	2.7	0.7	3.2	3–3.5

The measures values of $\bar{L}/D$ are means, with the standard deviation ('St. Dev.') also given for each material. The measured and reported values of E are means, with $E \pm \Delta$ indicating the range of measured values, and Δ indicating the range of reported values. PhG, phosphate glass; ChG, chalcogenide glass; TeG, tellurite glass; PEO, polyethylene oxide; PS, polystyrene. Reported values are from refs 42–56, as indicated.
[1]We did not measure E for the TeG used in our experiments. We produced polymer-TeG fibres by thermal co-drawing, which requires that the polymer and the glass have over-lapping softening temperatures T_{soft} (in our context, this refers to the temperature at which the viscosity drops to values compatible with thermal drawing, typically 10^4–10^6 Poise). All TeG materials reported in the literature have a T_{soft} that is substantially higher than that of engineering thermoplastic polymers such as PES. We modified the TeG composition to reduce T_{soft}. However, the TeG composition we used is hygroscopic; while the TeG is isolated from the ambient environment within the PES cladding, it remains stable; once the PES cladding is removed (to measure E), the TeG takes up moisture and becomes brittle. We expect that E is reduced when the T_{soft} of the material is reduced.
[2]We did not measure E for ice and instead plot in Fig. 2b the range of values that have been reported in the literature. This range is quite large, because E for ice depends on temperature, pressure, contaminants in the water, and so on. It is difficult to determine exactly the temperature of the ice during necking, but it is expected that the ice is in the process of melting and thus we estimate that E is on the lower end of the specified range.

Extended Data Table 2 | Comparison of simulated and measured (Fig. 2b) average value of *L/D* (denoted $\bar{L}/D$) and its standard deviation for different core materials

Core material	Simulations		Measurements	
	$\bar{L}/D$	St. Dev. in L/D	$\bar{L}/D$	St. Dev. in L/D
As_2Se_3	5.6	1.4	6	1.57
Si	36.6	5.9	32.5	9.56
Ge	30.9	5.4	30.0	9.26
Polystyrene (PS)	1.72	0.78	1.6	0.25

The cladding polymer is PES.